Global model comparison with Millstone Hill during September 2005

David J. Pawlowski,[1] Aaron J. Ridley,[1] Insung Kim,[2] and Dennis S. Bernstein[2]

Received 7 March 2007; revised 15 June 2007; accepted 1 October 2007; published 24 January 2008.

[1] A direct comparison between simulation results from the Global Ionosphere Thermosphere Model (GITM) and measurements from the Millstone Hill incoherent scatter radar (ISR) during the month of September 2005 is presented. Electron density, electron temperature, and ion temperature results are compared at two altitudes where ISR data is the most abundant. The model results are produced, first using GITM running in one dimension, which allows comparison at the Millstone Hill location throughout the entire month. The model results have errors ranging from 20% to 50% over the course of the month. In addition, the F2 peak electron density (NmF2) and height of the peak (HmF2) are compared for the month. On average the model indicates higher peak electron densities as well as a higher HmF2. During the time period from 9 September through 13 September, the trends in the data are different than the trends in the model results. These differences are due to active solar and geomagnetic conditions during this time period. Three-dimensional (3-D) GITM results are presented during these active conditions, and it is found that the 3-D model results replicate the trends in the data more closely. GITM is able to capture the positive storm phase that occurred late on 10 September but has the most difficulty capturing the density depletion on 11 and 12 September that is seen in the data. This is probably a result of the use of statistical high-latitude and solar drivers that are not as accurate during storm time.

Citation: Pawlowski, D. J., A. J. Ridley, I. Kim, and D. S. Bernstein (2008), Global model comparison with Millstone Hill during September 2005, *J. Geophys. Res.*, *113*, A01312, doi:10.1029/2007JA012390.

1. Introduction

[2] At low and middle latitudes, the major drivers and processes that dominate the quiet time ionosphere are reasonably well understood [*Torr et al.*, 1979; *Stolarski*, 1976; *Anderson and Roble*, 1981]. Ionization is controlled by the incoming solar extreme ultraviolet (EUV) flux and at low altitudes (100–150 km), where the background neutral density is relatively high, the ion production rates are at a maximum. Photoelectrons produced from the ionization are extremely important in this region since they lead to secondary ionization of the neutral gas [*Schunk and Nagy*, 1978]. The photoelectrons have very high velocities compared to the ions and thus do not transfer energy to the ions efficiently. Instead, the ions are influenced more by collisions with the neutrals as a result of the high neutral density. Therefore the ion temperatures are similar to the neutral temperature.

[3] At higher altitudes (above 250 km), the neutral density is sufficiently low enough that Coloumb interactions between the thermal electrons and ions become more important; thus the ion temperature begins to deviate from the neutral temperature. The lower neutral densities also result in slower recombination rates and therefore the chemical time constant increases with altitude. This means that the electron density is free to increase with altitude until the chemical time constant is greater than that for diffusion [*Schunk and Nagy*, 2000; *Rishbeth*, 1975, 1966].

[4] During active geomagnetic time periods, or geomagnetic storms, conditions in the ionosphere are much more dynamic [*Rishbeth et al.*, 1987; *Prölss*, 1997; *Mikhailov and Schlegel*, 1998]. Large amounts of energy are deposited in the high latitudes and magnetospheric electric fields vary rapidly, resulting in increased currents and enhanced particle precipitation. Additional energy deposited in the high latitudes creates equatorward directed neutral winds that push plasma in the *F* region up magnetic field lines. During active geomagnetic periods, the ionosphere tends to vary on extremely local scales.

[5] Much of the understanding of the ionospheric dynamics at midlatitudes was accomplished through the use of ISRs [*Evans*, 1971; *Roble*, 1975; *Schunk and Nagy*, 1978; *Baron and Wand*, 1983; *Kelly and Vickrey*, 1984]. These radars have the ability to determine the state of the ionosphere in a local region by obtaining electron density, electron and ion temperature, and ion velocity profiles. As radar data became readily available, global models of the ionosphere were developed to test our understanding of the system as a whole [*Fuller-Rowell and Rees*, 1980;

[1]Department of Atmospheric, Oceanic and Space Sciences, University of Michigan, Ann Arbor, Michigan, USA.
[2]Aerospace Engineering Department, University of Michigan, Ann Arbor, Michigan, USA.

0148-0227/08/2007JA012390

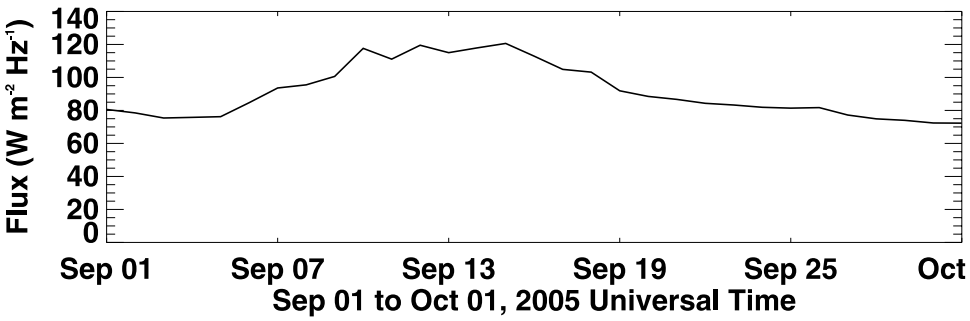

Figure 1. $F_{10.7}$ solar flux for the month of September 2005.

Buonsanto et al., 1999; *Lei et al.*, 2007]. Naturally, comparisons between models and radar data are important to determine how accurate these models are.

[6] Owing to the length of the experiments, incoherent scatter world months (ISWM) present excellent opportunities to perform comparisons between ISR data and global model results. September 2005 was one such month. Some of the goals of this ISWM were to study the lower thermosphere coupling in order to better understand tidal variability and to examine ionospheric variability and space weather effects. The length of the experiment allows for comparison of the model to data from a range of driving conditions. During this time period, the solar EUV conditions were quiet at the beginning of the month ($F_{10.7} \simeq 80$), became more active during the middle of the month ($F_{10.7} \simeq 120$), and then subsided at the end of the month (Figure 1). As a result of these solar variations, the Earth experienced a range of geomagnetic activity, including a geomagnetic storm, which began on 10 September (for detailed analysis of this storm, see *Goncharenko et al.* [2007]). Making comparisons during this period helps demonstrate when the model performs the best and provides insight as to what features of the model need additional attention. Also, long-term trends can be examined, such as changes due to $F_{10.7}$ over a few days to weeks. The ultimate goals of this study are to set a baseline for future comparisons between the model and data and to demonstrate the capabilities of GITM run in the most basic manner.

2. Data

[7] The Millstone Hill ISR system consists of a 2.5 MW peak UHF transmitter coupled to a 68-m zenith-directed fixed parabola antenna, as well as a fully steerable 46-m antenna. Measurement data from experiments are stored on the Madrigal internet-based database (http://www.openmadrigal.org), which serves data from several upper atmospheric science instruments.

[8] For this study, only data from the zenith antenna are used so the measurements are restricted to approximately 42° latitude and 288° longitude. Since the zenith antenna is fixed at an elevation angle of 88°, there is only a slight variation in the geographic coordinates of the measurements, depending on the height at which the measurement is taken. This variation, however, is much smaller than the typical 5° by 5° resolution used in global models. During the ISWM, the radar operated from 0800 UTC until 0000 UTC. Therefore only limited measurements are available of the nightside ionosphere. Also, for this study, data with a signal-to-noise ratio less than unity are removed from the set. While this is quite conservative, the filtering had minimal effect on the altitudes used in the study.

3. GITM Model Description

[9] The Global Ionosphere Thermosphere Model (GITM) is a three-dimensional spherical code that solves for the coupled ionosphere and thermosphere [*Ridley et al.*, 2006]. GITM differs from other global ionosphere-thermosphere models in that it uses an altitude grid rather than a pressure grid. GITM does not assume hydrostatic equilibrium, and thus nonhydrostatic solutions are possible. Furthermore, the user is free to specify the number of grid points used in a simulation, so the resolution of the model is free to change from run to run. As a result of this flexibility, the model can be run in one dimension, in which a single latitude and longitude are modeled and horizontal transport and gradients are ignored. External driving terms, such as the ionospheric potential, are specified on a 1° by 1° grid surrounding the one-dimensional (1-D) domain. *Deng and Ridley* [2006] described the ion advection in the high-latitude ionosphere and conducted simplified runs to show how GITM can develop vertical flows in the cusp region that may feed *F* region tongues of ionization.

[10] To calculate electron temperatures (T_e) within GITM, the electron energy equation is solved, neglecting chemical reactions as well as viscous heating. The loss processes taken into account include cooling due to rotational excitation of N_2 and O_2 as well as excitation of the fine structure levels of atomic oxygen [*Schunk and Nagy*, 2000]. At high temperatures, vibrational excitation of N_2, O_2, and electronic excitation of O are important and taken into account. At the lower boundary, the electron temperature (T_e) is set equal to the neutral temperature, while at the upper boundary (700 km for this study), the equation:

$$\frac{dTe}{dz} = \frac{Fe}{\kappa_e}$$

is used, where F_e is the heat flow rate specified by *Liemohn et al.* [2001], κ_e is Boltzmann's constant, and z is the altitude. Ion temperatures are calculated by assuming the

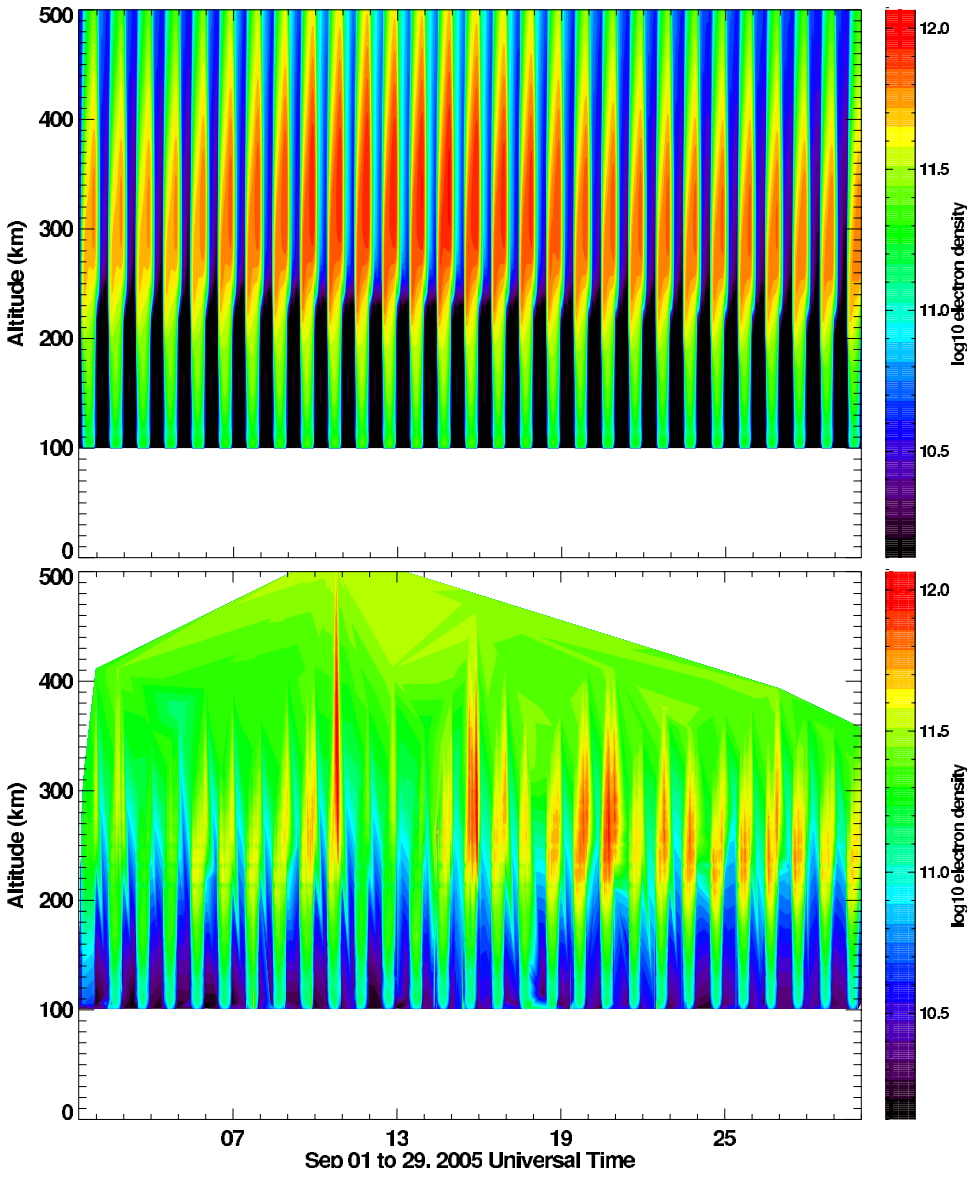

1

Figure 2. Altitude profile of election density versus time, showing (top) one-dimensional (1-D) Global Ionosphere Thermosphere Model (GITM) results and (bottom) Millstone Hill measurements.

energy gain from the electron-ion collisions, and other heating sources are balanced by the energy loss through ion-neutral collisions.

[11] Finally, GITM can output simulation results at the exact time and location that observational data is available. Thus GITM permits direct comparisons with data from both ground-based instruments as well as satellites. This feature is used to perform these comparisons.

[12] For this study, 1-D GITM is used to simulate the upper atmosphere for the duration of the ISWM. The main driver for Millstone Hill latitudes, the incident EUV flux, is derived using an $F_{10.7}$ proxy model [*Hinteregger et al.*, 1981; *Tobiska*, 1991]. In addition, 3-D GITM is used to perform a more realistic simulation of the geomagnetic storm that occurred on 10–13 September.

4. Results

4.1. Electron Density

[13] The electron density results from 1 September through 1 October from GITM along with the corresponding measurements from Millstone Hill are shown in Figure 2. The model results show a steady increase in electron density starting around 6 September, corresponding to an increase in

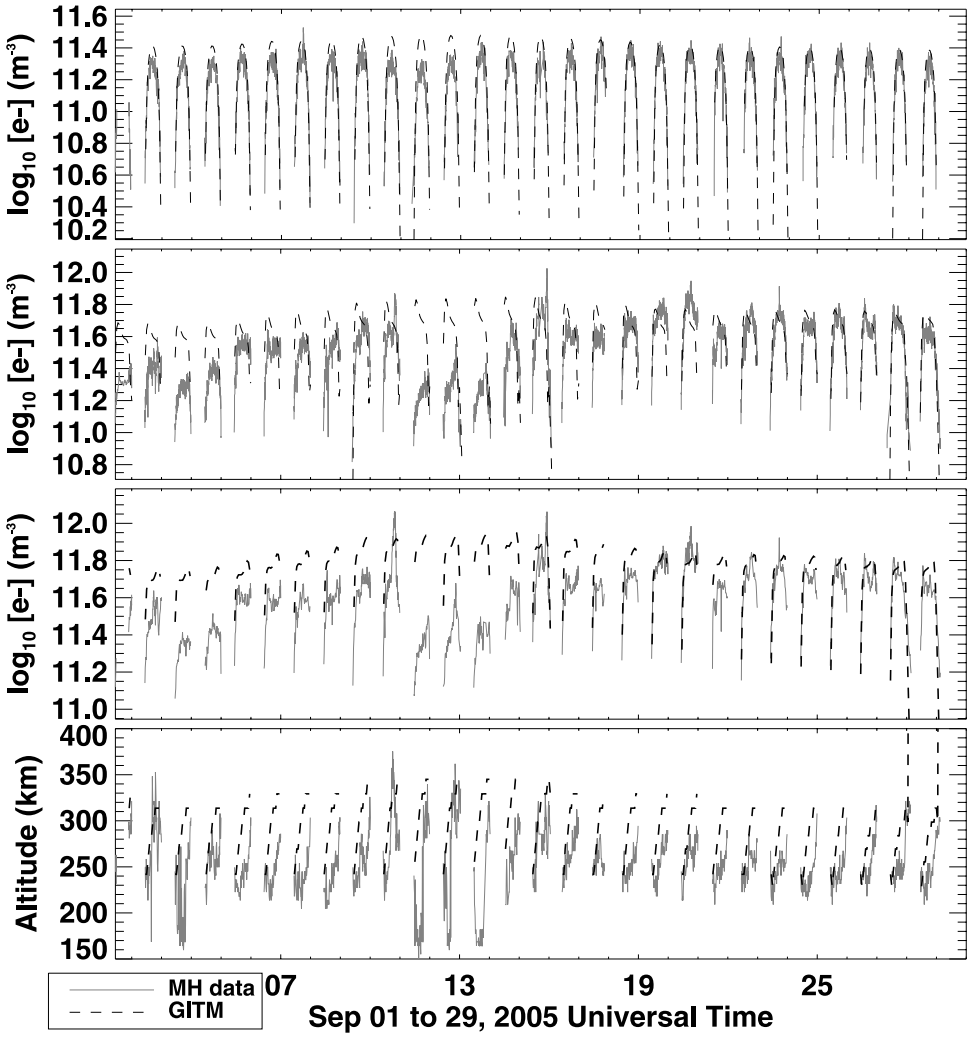

Figure 3. A comparison of electron densities at 155 km and 245 km using 1-D GITM results (dashed line) and Millstone Hill data (solid line) on a log scale. Also shown are comparisons between modeled and measured daily maximum electron concentration (NmF2) as well as the height of the maximum (HmF2).

the $F_{10.7}$ solar flux (Figure 1) during this time period. The solar flux peaks at 120.6×10^{-22} W m^{-2} Hz^{-1} on 15 September and then decreases slowly throughout the remainder of the month. The modeled electron densities closely follow the behavior of the $F_{10.7}$ during the month. The radar data, however, do not show the steady features that the model indicates, but rather indicate a relatively sharp increase in the electron density on 10 September, followed by a 3-d period during which the F_2 region is relatively weak.

[14] Figure 3 gives a more quantitative comparison of the data and the model results by showing the electron density as a function of time at two different altitudes. The log of the electron density versus time is plotted at 155 km and at 245 km. These altitudes are chosen because measurements are the most abundant. As mentioned previously, the Millstone Hill radar was not operated between 0000 and 0800 UT during the month. Consequently, the plots show several distinct lines rather than a single continuous one.

[15] The normalized RMS errors for electron density at 155 and 245 km are 28.5% and 47.7%, respectively, are shown in Table 1. Also shown are the errors in the electron temperature and ion temperature results. The normalized RMS error (E) is calculated using the formula:

$$E = \frac{\sqrt{\langle (F_{model} - F_{data})^2 \rangle}}{\sqrt{\langle F_{data}^2 \rangle}}$$

where $\langle\rangle$ symbolizes taking a mean, and F is the density or temperature. At E = 0, the model and data agree perfectly, while at E = 1, the model could be replaced by a zero line. With values of E greater than 1, the model results are diverging from the data, and most likely the model does not trend with the data. The model and the data compare the best at the beginning and end of the month and differ the most during the storm period. The errors during the storm are exaggerated at 245 km, where there is a maximum difference of nearly a factor of 5. At this altitude, the maximum daily electron density from GITM steadily increased by 41% between 5 and 12 September, when the $F_{10.7}$ peaked. As the solar and geomagnetic conditions

Table 1. Normalized RMS Errors for Electron Density, Temperature, and Ion Temperature at 155 and 245 km[a]

	155 km	245 km
n_e	0.285	0.477
T_e	0.192	0.340
T_i	0.213	0.152

[a]Normalized RMS error is calculated by taking the RMS of the data subtracted from the model results and then dividing by the RMS of the data.

quieted, the maximum electron density decreased and levelled off at around 5.5×10^{11} m^{-3}. Similarly, the Millstone Hill data at 245 km shows a 31% increase in maximum electron density between 5 and 9 September due to the increasing solar flux. However, the maximum density increases from 5.70×10^{11} m^{-3} on 9 September to 7.41×10^{11} m^{-3} on 10 September, an additional 30% increase over the course of 1 d. GITM clearly does not capture this rise. Also, on 11 September, the Millstone observations show the maximum density at 245 km to decrease by a factor of five, a feature not seen in the model results.

[16] These differences are also observed in the plot of the peak electron density (NmF2) for the month. The ISR data show a substantial increase in the maximum NmF2 density between 9 September and 10 September from 5.83×10^{11} m^{-3} to 1.16×10^{12} m^{-3}, followed by a large drop in density on 11 September to 3.2×10^{11} m^{-3}. During these 3 d, the model results show the NmF2 to remain nearly constant.

[17] The altitude of the *F*2 peak (HmF2) is also plotted in Figure 3. The model results show, on average, the HmF2 to be 46 km, or 14.8% higher than the observed altitude. One of the most interesting features in the data is that the *F*2 region is extremely variable during 11 September. There are periods during which the data indicate HmF2 drops to near 150 km. The altitude profile in Figure 2 indicates that during this time period, the *F*2 region seems to nearly disappear.

4.2. Electron Temperature

[18] Electron temperatures are plotted in Figures 4a and 4b, again at altitudes of 155 km and 245 km, respectively. Similar to the electron density results, the model performs better at lower altitudes, where there is, on average, a normalized RMS of 19.2% between the modeled and measured temperatures. At 245 km, the average error is 34.0% over the duration of the month. However, at 245 km, during the period of active geomagnetic conditions, the behavior of the data is different from that of the model. The Millstone Hill data show a distinct drop in the dayside electron temperature from 10 September with a recovery on 11 September. GITM results show a steadily increasing temperature during this period as a result of the increased incident energy flux.

4.3. Ion Temperature

[19] Ion temperature results and measurements for the month are shown in Figures 5a and 5b at 155 and 245 km, respectively. The model has a normalized RMS of 21.3% at 155 km and 15.2% at 245 km compared to the measured ion temperatures. The model calculates the average daily temperature at 155 and 245 km to be 714.9 and 880.3 K, respectively. These values are consistent with the observed 706.8 and 885.8 K at the respective lower and higher altitude. The most significant difference between the observations and model results is when the peak in the ion temperature occurs. At 155 km, the model indicates that the ion temperature peaks on average, after 2100 UT. The observations indicate the ion temperature to peak much earlier, just after 1600 UT.

5. Three-Dimensional Comparison With the Storm

[20] Geomagnetic storms affect the ionosphere on global scales. The large amounts of energy that are deposited in the high latitudes may result in traveling ionospheric disturbances (TIDs), equatorward propogating waves, and composi-

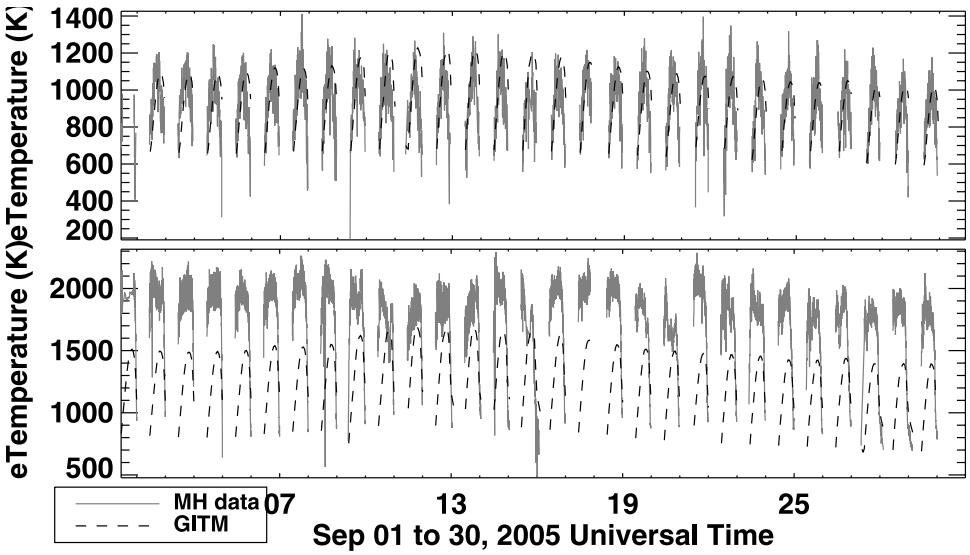

Figure 4. Electron temperatures at (top) 155 km and (bottom) 245 km from 1-D GITM (dashed line) and Millstone Hill data (solid line).

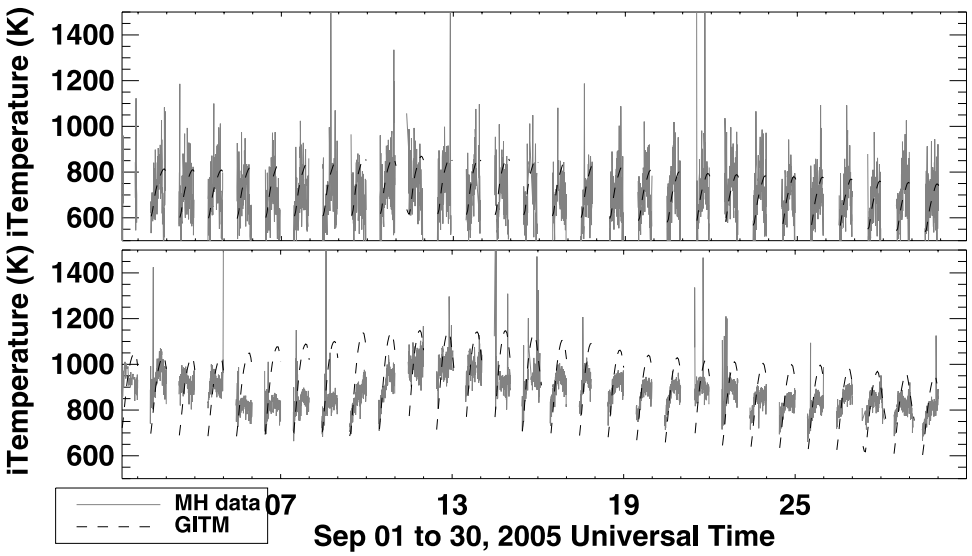

Figure 5. Ion temperatures at (top) 155 km and (bottom) 245 km from 1-D GITM (dashed line) and Millstone Hill (solid line).

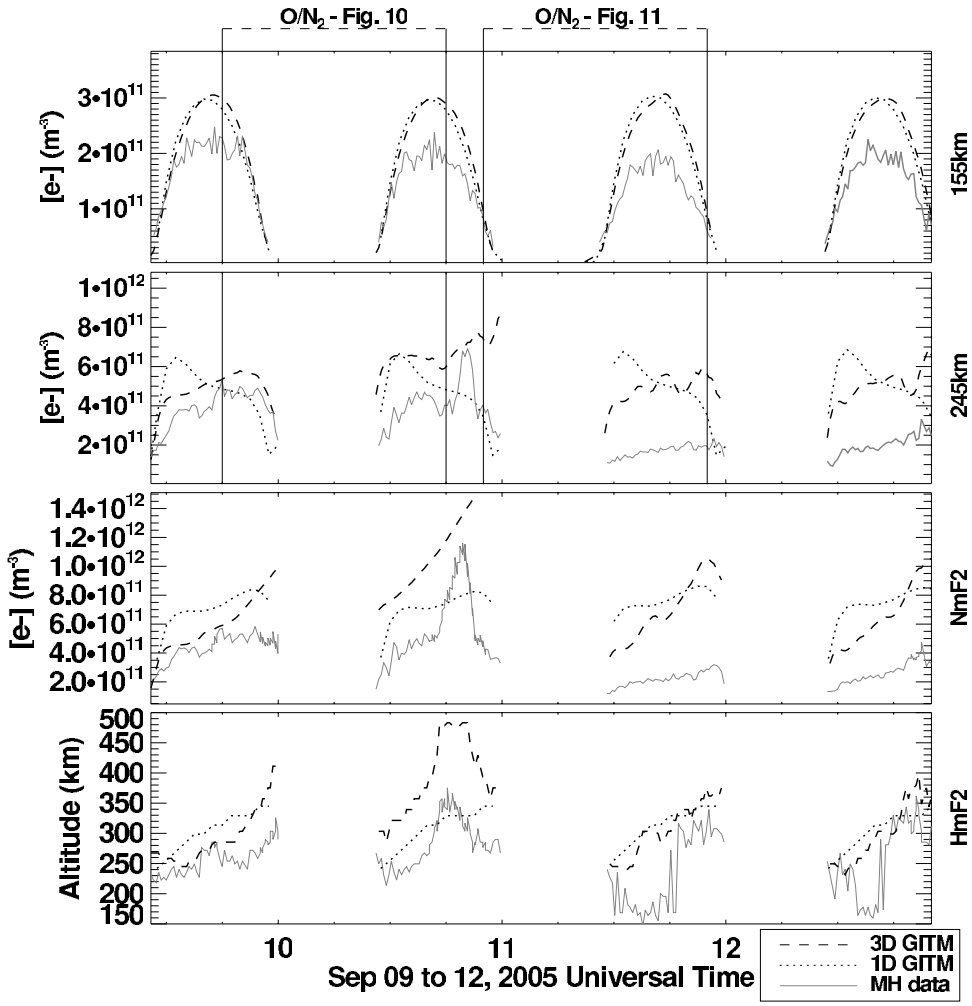

Figure 6. GITM results and Millstone Hill data (solid line) for 9 September 2005 through 12 September 2005 at 155 km and 245. Also shown are NmF2 and HmF2 from the model and data. Both 3-D (dotted line) and 1-D (dashed line) results are plotted on a linear scale.

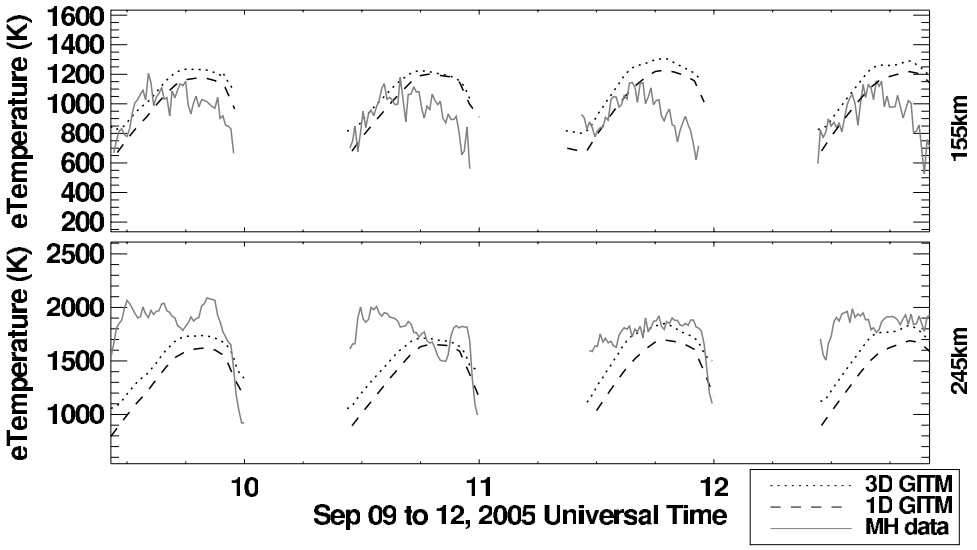

Figure 7. GITM results and Millstone Hill data (solid line) for 9 September 2005 through 12 September 2005 at (top) 155 km and (bottom) 245 km. Both 3-D (dotted line) and 1-D (dashed line) electron temperatures are plotted.

tion advection. For this reason, it is not possible to capture the physics over Millstone Hill during a storm if the global dynamics are not included. By running in 1-D, the effects of the increased high-latitude energy input are not propagated to the Millstone Hill region. In order to more accurately take into account the effects of the storm, a comparison between GITM run in 3-D and the ISR data is also performed. The Weimer ionospheric potential model [*Weimer*, 1996] and a $F_{10.7}$ proxy are used as high latitude and solar drivers, and the ionosphere-thermosphere system is simulated using a 2.5° latitude by 5° longitude grid.

[21] Figures 6, 7 and 8 show the electron density, temperature, and ion temperature results and data, respectively, from 9 through 13 September. One-dimensional (solid red line) and 3-D (dashed red line) GITM results are shown along with the Millstone Hill data (black line). In Figure 6 the electron densities are plotted on a linear scale at 155 and 245 km and the normalized RMS errors over the course of the 4-d period are given in Table 2. Even though 1-D GITM results in lower normalized RMS errors (i.e., a quantitatively better solution) for (1) electron densities at both altitudes, (2) electron temperatures at 155 km, (3) and ion temperatures at 245 km, the model run in 3-D does a better job of capturing the trends and dynamic behavior during the storm.

[22] To evaluate how the two runs compare to the overall behavior of the data, a cross correlation is performed between both 1-D and 3-D GITM results and the data. Table 2 shows the cross-correlations at 155 km and 245 km for the electron

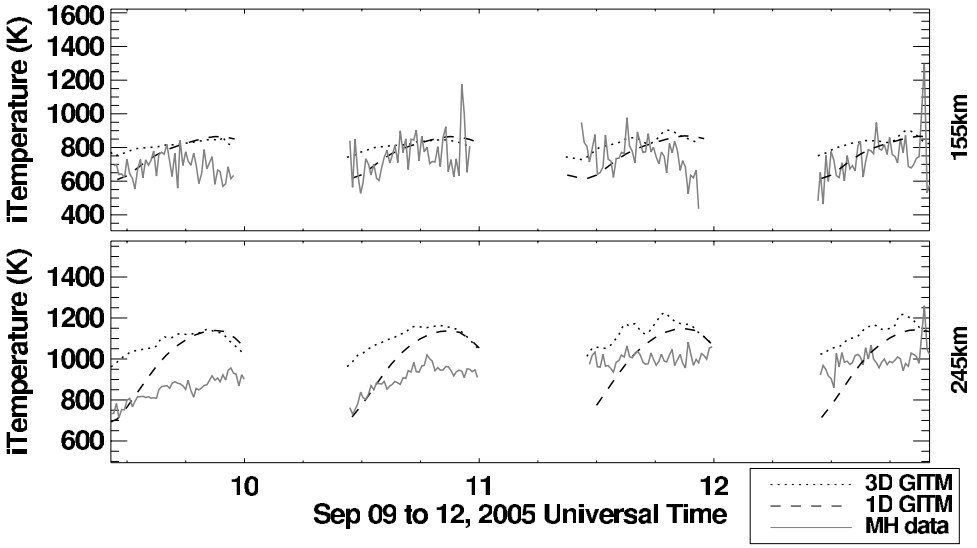

Figure 8. GITM results and Millstone Hill data (solid line) for 9 September 2005 through 12 September 2005 at (top) 155 km and (bottom) 245 km. Both 3-D (dotted line) and 1-D (dashed line) ion temperatures are plotted.

Table 2. Normalized RMS Errors and Cross-Correlation Between One-Dimensional (1-D) and 3-D Global Ionosphere Thermosphere Model Results and Data for Electron Density, Temperature, and Ion Temperature at 155 and 245 km During the Storm[a]

	Normalized RMS				Cross-Correlation			
	3-D		1-D		3-D		1-D	
	155 km	245 km	155 km	245 km	155 km	245 km	155 km	245 km
n_e	.443	.854	.429	.774	.933	.552	.919	.027
T_e	.251	.197	.202	.275	.428	.267	.375	.278
T_i	.199	.201	.203	.157	.118	.649	.123	.508

[a]Normalized RMS error is calculated by taking the RMS of the data subtracted from the model results and then dividing by the RMS of the data.

density and temperature and the ion temperature. The cross-correlations for the electron densities at 155 km are very similar for 1-D and 3-D GITM. At 245 km, the correlations are not nearly as similar, as can be seen by eye in the second panel of Figure 6. At this altitude, the cross correlation is 0.027 for 1-D and 0.552 for 3-D GITM. In addition, Figure 6 shows a comparison of NmF2 and HmF2. Using 3-D GITM, the cross correlations between the model and data is 0.634 and 0.554 for NmF2 and HmF2, respectively. In both cases, this is a significant improvement over 0.262 and 0.203 obtained from 1-D GITM. The electron temperature at 155 km and the ion temperature at 245 km calculated by 3-D GITM also have higher cross correlations than those calculated by 1-D GITM.

[23] It should be noted that late on 10 September, the HmF2 is near the top boundary of the model. At this altitude, the plasmasphere is a source of plasma to the ionosphere due to the downward ion velocities (Figure 9) and thus during this time the electron density is nearly constant with altitude above 350 km. Early on 11 September, there are significant upward velocities throughout the

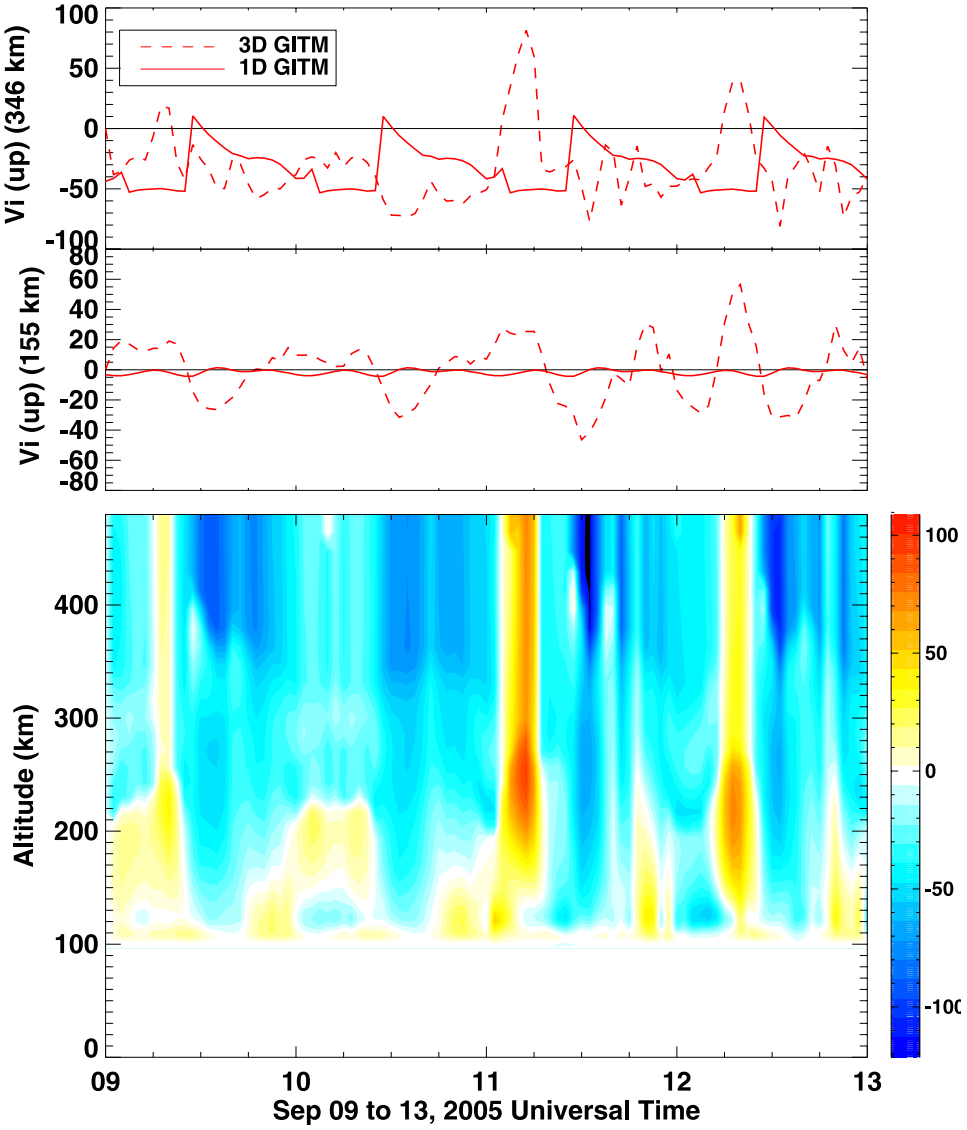

Figure 9. Vertical ion velocity results from GITM above Millstone Hill as a function of time. Positive values are up and negative are down.

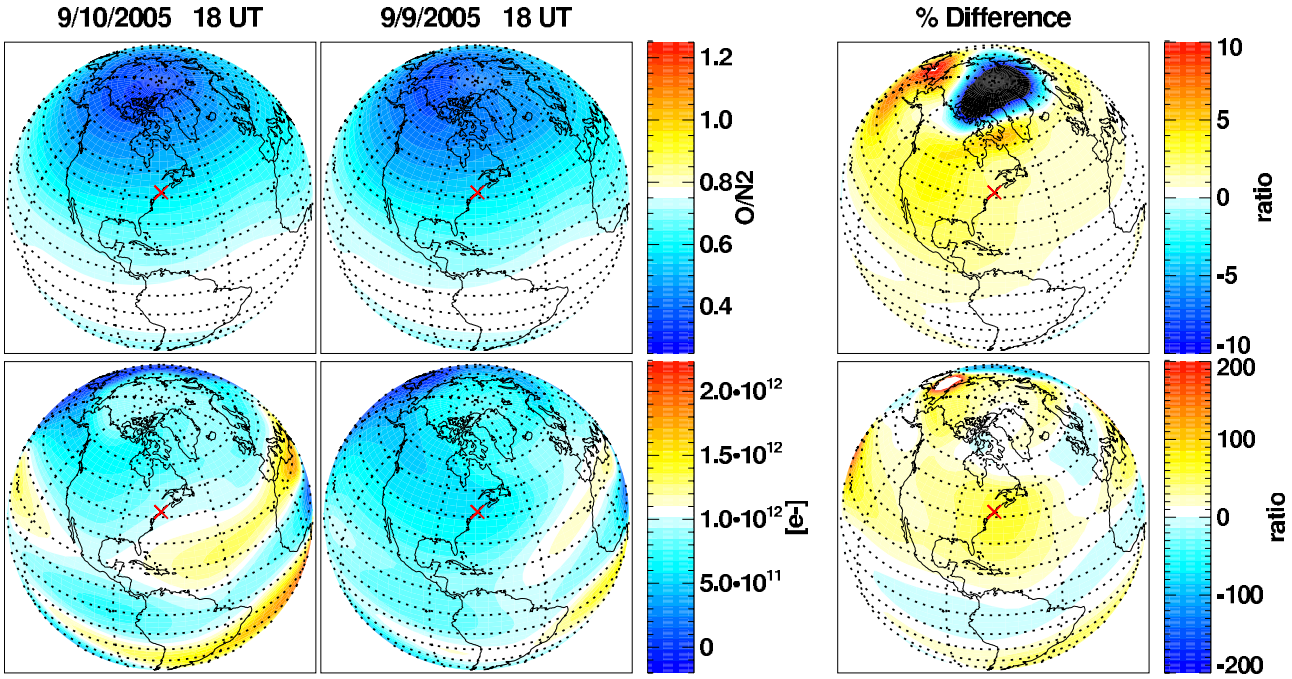

Figure 10. Comparison of (top) O/N_2 and (bottom) electron density at 1800 UT between (left) 10 September and (middle) 9 September. The ratio between the 2 d is plotted on the right.

ionosphere, which push the plasma out the top boundary and bring the *F*2 layer back to a normal altitude.

[24] On 10 September the simulated (3-D) and observed peak electron densities are enhanced compared to the electron densities on 9, 11, and 12 September. Late on 10 September, a positive phase ionospheric storm occurs over the Millstone Hill site, driving the densities even higher. Previous studies indicate that this positive storm is primarily a result of the convergence of upward and downward plasma flow near the *F*2 peak [*Goncharenko et al.*, 2007]. Three-dimensional GITM also indicates that this increase is primarily a result of convergence. Figure 9 shows the altitude profile the vertical ion velocity at Millstone Hill. After about 1800 UT on 10 September, there are significant upward flows below about 160 km and significant downward flows above 180 km. Even though the height of the *F*2 layer during this time is above this region of zero flow, the model indicates there are sharp vertical gradients in the downward velocity throughout the *F* region. These gradients are causing plasma to pile up in the *F* region and also causing the HmF2 to be highly variable. This mechanism is also contributing to the density increase late on 9 September, where there is a clear upward trend in the vertical velocity profile (which corresponds to an upward trend in HmF2 (Figure 6)).

[25] In addition to convergence, 3-D GITM indicates that compositional changes are also influencing the electron density on 10 September. Figure 10 shows a comparison of the integrated O/N_2 ratio between 1800 UT on 9 September and 1800 UT on 10 September in the region surrounding Millstone Hill. The integrated O/N_2 ratio is calculated by integrating both the [O] and [N_2] downward from the top of the model, until the integral of [N_2] reaches a value of 1×10^{21} m^{-2}. The ratio of the two concentrations is then taken. The top two panels show O/N_2 ratios on 9 September (right) and 10 September (left), respectively, while the bottom panel shows the ratio of the 2 d, which is calculated using the equation:

$$\frac{O/N_2(10) - O/N_2(9)}{O/N_2(9)} \times 100$$

where O/N_2 on 10 September is denoted as $O/N_2(10)$. The bottom panel indicates that the O/N_2 ratio near Millstone Hill on 10 September is larger than the O/N_2 ratio on 9 September. This means that the loss of electrons due to dissociative recombination with N_2 is slower on 10 September than on 9 September. Therefore it is expected that the electron density would be higher on 10 September. Figure 11 shows the same format as Figure 10, except 2200 UT on 10 September (right) and 11 September (left) are plotted. The bottom panel suggests that over Millstone Hill, O/N_2 ratio is lower on 11 September, implying that the electron density should be lower on 11 September. The changes in O/N_2 ratio are a result of the heating in the high-latitude region, and the transport of the temperature and composition changes to midlatitudes. *Goncharenko et al.* [2007] also find that composition may affect the enhancement on 10 September; however, they suggest that the vertical velocities must play a more significant role because of the variability of HmF2.

[26] On 11 and 12 September, the observed electron densities are depleted from their prestorm values. The model, however, does not show any depletion. Other models have shown that these negative storm effects at midlatitudes may be attributed to further compositional changes being deposited in this region from higher latitudes [*Fuller-Rowell et al.*, 1994, 1996; *Burns et al.*, 1991]. A

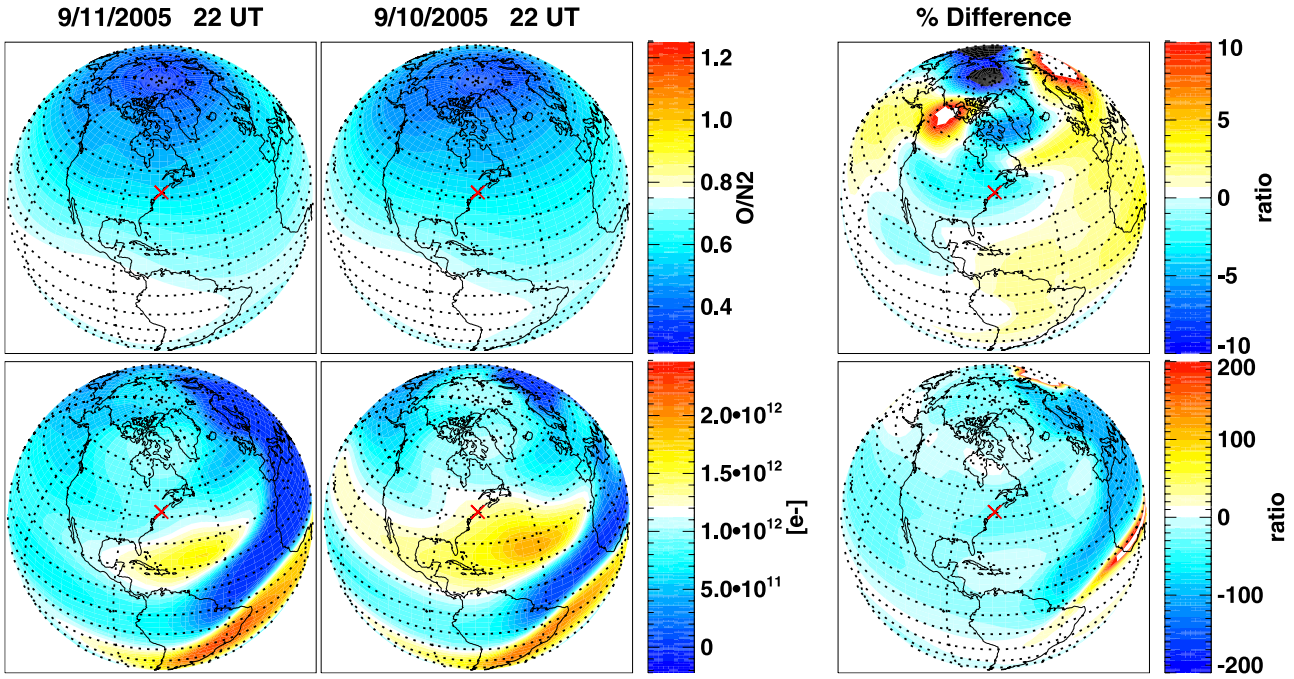

Figure 11. The same as Figure 10 only for 2200 UT on (left) 11 September and (middle) 10 September.

likely explanation for the lack of density depletion is that there is not enough horizontal momentum carrying this disturbance from high latitudes to midlatitudes. Making use of more realistic high-latitude drivers may result in more significant equatorward winds after the main phase of the storm, upwelling low O/N_2 air into the *F* region, and causing a drop in the electron density.

6. Discussion and Conclusions

[27] The 1-D model results indicate that over the course of the month, GITM performs better at 155 km, where the ionosphere is strongly driven by the solar EUV inputs, and transport is not as important. The normalized RMS error between the modeled and observed electron densities is 28.5% at this altitude, and the normalized RMS between the modeled and measured electron and ion temperatures is 19.2% and 21.3%, respectively. At 245 km, the electron density and electron temperature have larger errors than at lower altitudes (47.7% and 34.0% normalized RMS); however, the ion temperature RMS error, 15.2%, is lower at higher altitude. The larger error in the density and temperature is expected, since horizontal dynamics (not modeled in 1-D) are starting to play a significant role at 245 km.

[28] The largest differences between the data and the model results occur during the geomagnetic storm. Specifically, on 10 September, 1-D GITM shows a steady increase in NmF2, HmF2, and electron and ion temperatures in the F2 region. However, the measured electron densities increase only slightly, until late on 10 September, when there is a sharp increase in density as well as in the HmF2. The increased electron density results in a drop in electron temperature in the *F* region, since, as the electron density increases, the thermal conductivity increases, allowing more energy to be lost to the cooler medium below [*Banks*, 1969].

[29] The 3-D results show improvement in capturing the variability in the ionosphere during the active conditions. Interestingly, the RMS errors are larger in 3-D in some results than they are using 1-D GITM. However, when compared to the data, the 3-D results show improvements in the overall trends in the ionosphere.

[30] The improved behavior of 3-D GITM is most obvious in the electron density results, especially in the *F* region. The 3-D GITM shows overall enhanced electron densities on 10 September and also captures the positive phase storm, as observed in the data, and suggests that the enhancement late on 10 September is a result of sharp gradients in the vertical velocity, causing convergence of plasma flow, in agreement with *Goncharenko et al.* [2007]. GITM also suggests that the transport of molecular poor (low N_2) air into the ionosphere above Millstone Hill may also play a role [*Burns et al.*, 1989, 1995; *Rishbeth*, 1975], but a less significant one.

[31] The cross correlation analysis shows that in four of the six cases, 3-D GITM is capturing the overall trends in the data better than 1-D GITM. One of the cases that did not show improvement was the ion temperature at 155 km. As it turns out, this altitude is in the middle of the molecular to atomic oxygen ion transition. In order to obtain ion temperatures in this region, assumptions about the ion composition are made here that can be violated during storm time, which may have contributed to the differences between the data and the model. In cases such as this, first principle models could greatly assist in performing calculations to provide better estimates of the parameters.

[32] Ultimately, the cross correlations indicate that it is necessary to take into account horizontal dynamics in order to accurately simulate the ionosphere, as expected. At lower altitudes, much of the small-scale variability is not captured by either 1-D or 3-D GITM. This variability is seen in the

data, partially because at lower altitudes, the chemical time constants are small, and therefore the ionsphere reacts quickly to changes in the incident solar flux. In both simulations the solar flux has been specified by the $F_{10.7}$ proxy, which is updated once per day. Incorporation of a high time resolution spectrum may add more variability into the model results, pushing it toward what is observed in the data.

[33] This work shows that 1-D GITM can reproduce the midlatitude ionospheric state to a 20–30% accuracy over an entire month. The 1-D model has the most difficulty when there are active solar and geophysical conditions, in part because horizontal gradients were ignored. During these periods, it is necessary to incorporate global dynamics in order to more accurately capture the variability in the ionosphere. In a future study, more realistic high latitude and solar drivers will be used to simulate the September 2005 storm. By comparing those results to multiple ISRs, as well as data from other instruments such as the Global Ultraviolet Imager (GUVI) [*Christensen et al.*, 2003] and the Challenging Minisatellite Payload (ChaMP) [*Reigber et al.*, 2000], it will be possible to understand, in more detail, where the model needs further improvement and to better understand the controlling physical processes.

[34] **Acknowledgments.** The authors would like to thank those involved with Millstone Hill and the Madrigal database for making observational data readily available. Also, the useful comments from Larisa Goncharenko are much appreciated. This study was supported in part by NSF grants 0539053 and 0639336.

[35] Zuyin Pu thanks Alan G. Burns and another reviewer for their assistance in evaluating this paper.

References

Anderson, D. N., and R. G. Roble (1981), Neutral wind effects on the equatorial F-region ionosphere, *J. Atmos. Terr. Phys.*, *43*, 835.

Banks, P. M. (1969), The thermal structure of the ionosphere, *Proc. IEEE*, *57*(3), 258.

Baron, M. J., and R. H. Wand (1983), *F* region ion temperature enhancements resulting from Joule heating, *J. Geophys. Res.*, *88*, 4114.

Buonsanto, M. J., S. A. González, G. Lu, B. W. Reinisch, and J. P. Thayer (1999), Coordinated incoherent scatter radar study of the January 1997 storm, *J. Geophys. Res.*, *104*, 24,625.

Burns, A. G., T. L. Killeen, G. Crowley, B. A. Emery, and R. G. Roble (1989), On the mechanisms responsible for high latitude thermospheric composition variations during the recovery phase of a geomagnetic storm, *J. Geophys. Res.*, *94*, 16,961.

Burns, A. G., T. L. Killeen, and R. G. Roble (1991), A simulation of thermospheric composition changes during an impulsive storm, *J. Geophys. Res.*, *96*, 14,153.

Burns, A. G., T. L. Killeen, G. R. Carignan, and R. G. Roble (1995), Large enhancements in the O/N_2 ratio in the evening sector of the winter hemisphere during geomagnetic storms, *J. Geophys. Res.*, *100*, 14,661.

Christensen, A. B., et al. (2003), Initial observations with the Global Ultraviolet Imager (GUVI) in the NASA TIMED satellite mission, *J. Geophys. Res.*, *108*(A12), 1451, doi:10.1029/2003JA009918.

Deng, Y., and A. J. Ridley (2006), Dependence of neutral winds on convection E-field, solar EUV, and auroral particle precipitation at high latitudes, *J. Geophys. Res.*, *111*, A09306, doi:10.1029/2005JA011368.

Evans, J. V. (1971), Observations of *F* region vertical velocities at Millstone Hill, 1, Evidence for drifts due to expansion, contraction and winds, *Radio Sci.*, *6*, 609.

Fuller-Rowell, T. J., and D. Rees (1980), A three-dimensional, time-dependent, global model of the thermosphere, *J. Atmos. Sci.*, *37*, 2545.

Fuller-Rowell, T. J., M. V. Codrescu, R. J. Moffett, and S. Quegan (1994), Response of the thermosphere and ionosphere to geomagnetic storms, *J. Geophys. Res.*, *99*, 3893.

Fuller-Rowell, T. J., D. Rees, S. Quegan, R. J. Moffett, M. V. Codrescu, and G. H. Millward (1996), *Solar-Terrestrial Energy Program: Handbook of Ionospheric Models*, edited by R. W. Schunk, p. 217, AGU, Washington, D. C.

Goncharenko, L. P., J. Foster, A. Coster, C. Huang, N. Aponte, and L. Paxton (2007), Observations of a positive storm phase on September 10, 2005, *J. Atmos. Sol. Terr. Phys.*, *69*, 1253, doi:10.1016/j.jastp.2006.09.001.

Hinteregger, H. E., K. Fukui, and B. R. Gibson (1981), Observational, reference and model data on solar EUV from measurements on AE-E, *Geophys. Res. Lett.*, *8*, 1147.

Kelly, J. D., and J. F. Vickrey (1984), F-region ionospheric structure associated with antisunward flow near the dayside polar cusp, *Geophys. Res. Lett.*, *11*, 907.

Lei, J., R. G. Roble, W. Wang, B. A. Emery, and S. Zhang (2007), Electron temperature climatology at Millstone Hill and Arecibo, *J. Geophys. Res.*, *112*, A02302, doi:10.1029/2006JA012041.

Liemohn, M. W., J. U. Kozyra, M. F. Thomsen, J. L. Roeder, G. Lu, J. E. Borovsky, and T. E. Cayton (2001), The dominant role of the asymmetric ring current in producing the stormtime D_{st}*, *J. Geophys. Res.*, *106*, 10,883.

Mikhailov, A., and K. Schlegel (1998), Physical mechanism of strong negative storm effects in the daytime ionospheric *F*2 region observed with EISCAT, *Ann. Geophys.*, *16*, 602.

Prölss, G. W. (1997), Magnetic storm associated perturbations of the upper atmosphere, in *Magnetic Storms*, *Geophys. Monogr. Ser.*, vol. 98, edited by B. T. Tsurutani et al., p. 227, AGU, Washington, D. C.

Reigber, C., H. Luhr, and P. Schwintzer (2000), CHAMP mission satus and perspectives, *Eos. Trans. AGU*, *81*(48), Fall Meet. Suppl., F307.

Ridley, A. J., Y. Deng, and G. Toth (2006), The global ionosphere-thermosphere model, *J. Atmos. Sol. Terr. Phys.*, *68*, 839.

Rishbeth, H. (1966), *F*2-layer rates at sunspot minimum, *J. Atmos. Terr. Phys.*, *28*, 911.

Rishbeth, H. (1975), *F*-region storms and thermospheric circulation, *J. Atmos. Terr. Phys.*, *37*, 1055.

Rishbeth, H., T. J. Fuller-Rowell, and A. D. Rodger (1987), *F*-layer storms and thermospheric composition, *Phys. Scr.*, *36*, 327.

Roble, R. G. (1975), The calculated and observed diurnal variation of the ionosphere over Millstone Hill on 23–24 March 1970, *Planet. Space Sci.*, *23*, 1017–1033, doi:10.1016/0032-0633(75)90192-0.

Schunk, R. W., and A. F. Nagy (1978), Electron temperatures in the *F*-region of the ionosphere, *Rev. Geophys.*, *16*, 355.

Schunk, R. W., and A. F. Nagy (2000), *Ionospheres*, Cambridge Univ. Press, New York.

Stolarski, R. S. (1976), Energetics of the midlatitude thermosphere, *J. Atmos. Terr. Phys.*, *38*, 863.

Tobiska, W. K. (1991), Revised solar extreme ultraviolet flux model, *J. Atmos. Terr. Phys.*, *53*, 1005.

Torr, D. G., et al. (1979), An experimental and theoretical study of the mean diurnal variation of O^+, NO^+, O_2^+, and N_2^+ ions in the mid-latitude *F*1 layer of the ionosphere, *J. Geophys. Res.*, *84*, 3360.

Weimer, D. R. (1996), A flexible, IMF dependent model of high-latitude electric potential having "space weather" applications, *Geophys. Res. Lett.*, *23*, 2549.

D. S. Bernstein and I. Kim, Aerospace Engineering Department, University of Michigan, Ann Arbor, MI 48109-2143, USA.

D. J. Pawlowski and A. J. Ridley, Department of Atmospheric, Oceanic and Space Sciences, University of Michigan, Ann Arbor, MI 48109-2143, USA. (dpawlows@umich.edu)